Bottom-up Quasi-Epitaxial Growth of Hybrid Perovskite from Solution Process – Achieving High-Efficiency Solar Cells via Template Guided Crystallization

Hengkai Zhang[1,2,†], Minchao Qin[3,†], Zhiliang Chen[1], Wei Yu[1,5], Zhiwei Ren[1,2], Kuan Liu[1,2], Jiaming Huang[1,2], Yaokang Zhang[4], Qiong Liang[1,2], Patrick W.K. Fong[1], Hrisheekesh Thachoth Chandran [1,2], Zijian Zheng[4], Xinhui Lu[3*], Gang Li[1,2*]

Affiliations:

[1]Department of Electronic and Information Engineering, Research Institute for Smart Energy (RISE), The Hong Kong Polytechnic University, Hung Hom, Kowloon, Hong Kong, China

[2]The Hong Kong Polytechnic University Shenzhen Research Institute, Shenzhen 518057, China

[3]Department of Physics, The Chinese University of Hong Kong, New Territories, Hong Kong, China

[4]Laboratory for Advanced Interfacial Materials and Devices, Research Centre for Smart Wearable Technology, Institute of Textiles and Clothing, The Hong Kong Polytechnic University, Hung Hom, Kowloon, Hong Kong, China

[5]State Key Laboratory of Catalysis, Dalian Institute of Chemical Physics, Chinese Academy of Sciences, Dalian National Laboratory for Clean Energy, Dalian 116023, Liaoning, China

†These authors contributed equally to this work.

* Correspondence author. Email: gang.w.li@polyu.edu.hk (G.L.); xhlu@phy.cuhk.edu.hk (X.L.)

Abstract:

Epitaxial growth gives the highest-quality crystalline semiconductor thin films for optoelectronic devices. Here we report a universal solution-processed bottom-up quasi-epitaxial growth of highly oriented α-$FAPbI_3$ perovskite film via a two-step method, in which the crystal orientation of α-$FAPbI_3$ film was precisely controlled through the synergetic effect of MACl and large-organic cation BABr etc. *In situ* GIWAXS visualizes the BA-related intermediate phase formation at the bottom, which serves as a guiding template for the bottom-up quasi-epitaxial growth in the subsequent annealing process. The template-guided epitaxial-grown BAFAMA perovskite film exhibit increased crystallinity, preferred crystallographic orientation, and reduced defects. ~~The resultant BAFAMA perovskite solar cell delivers an enhancement of the power conversion efficiency up to 22.7% (with steady power output of 22.3% PCE), associated with a significant 70 mV V_{OC} enhancement.~~ Moreover, the BAFAMA perovskite solar cells demonstrate decent stability, maintaining 95% of initial PCE after 2600h ambient storage, and 5-time operation condition lifetime enhancement.

Introduction

Organic-inorganic metal halide perovskite solar cell has attracted keen attention and came out as one of the most promising research topics in material science for its low-cost, solution-processed fabrication and excellent optoelectronic properties [1]. As the benchmark, conventional three-dimensional perovskite has been extensively studied, and great efficiency progress has been achieved since the seminal paper in 2009 [2], through the optimization of device structure [3], fabrication techniques modification [4], interface engineering [5], and composition engineering [6]. The power conversion efficiency (PCE) of perovskite solar cells has raised from 3.8% [2] to a certified 25.5% PCE in 2020 [7]. To further enhance the photovoltaic performance, precise and delicate control over the perovskite crystal structure and arrangement are urgently needed to go forward.

Epitaxial growth is often viewed as the ultimate technique to obtain the highest-quality crystalline semiconductor film through the ordered growth on the preferred single crystalline substrate [8]. The term epitaxy is derived from Greek, where epi means above or over, and taxy means order or arrangement. The crystalline orientation of deposited thin film is highly dependent on the substrate. The epitaxial growth has presented its great success in high-performance III-V semiconductor materials (e.g., GaAs, GaInP, AlGaInP, AlInP, and GaN) for optoelectronic devices [9]. Compared with classical molecular beam epitaxy (MBE), epitaxial CVD, or atomic layer epitaxy/deposition, liquid-phase epitaxy has clear advantages on device manufacture (inexpensive equipment setup, no rigorous operation requirement: high vacuum and high temperature), while so far, the quality control is not satisfactory due to poor uniformity and rough surface morphology, particularly in thin-film electronic devices [8]. Recently, the solution-processed epitaxial growth has been reported to obtain high-quality perovskite thin film with reduced defect density and excellent photovoltaic property [10]. The majority of the proposed epitaxial grown perovskites relied on an exterior template: either a single crystalline substrate such as alkali halide [10a, 10d], ZnSe [10g], or conventional glass substrates modified by 2D material such as MoS_2 [10b] and WS_2 [10e] or polymer template[11]. Apart from the exterior template-guided epitaxial perovskite film, the localized epitaxial growth of perovskite film has also been reported [12]. The exterior template-guided and localized epitaxial growth has been shown and explained through static measurements (mainly TEM) and DFT simulation. The understanding of the epitaxial crystallization kinetics, however, is very limited so far.

In this work, we first demonstrate a solution-processed bottom-up quasi-epitaxial perovskite growth through a synergetic effect of methylammonium chloride (MACl) additive and large-organic cation. Then we systematically investigate the crystallization kinetics of the perovskite quasi-epitaxial growth through a simple two-step method [13], which leads to the highly oriented quasi-epitaxial α-$FAPbI_3$ film. The *in situ* and *ex situ* GIWAXS measurements have been conducted to visualize the crystallization dynamic of solution-processed quasi-epitaxial growth of the α-$FAPbI_3$ film. From the *in situ* GIWAXS measurements, the n-butylammonium (BA)-based intermediate phase is proven to grow preferably at the bottom of the intermediate layer. The depth-resolved *ex situ* GIWAXS results provide clear evidence of bottom-up perovskite growth during

the annealing process, which is the prerequisite of template guided epitaxial growth. The bottom BA-related intermediate phase is first converted into an oriented template, followed by a slow self-assembly process (MACl enabled) which guides the quasi-epitaxial growth of perovskite film from the bottom to the top. The solution-processed bottom-up quasi-epitaxial growth of perovskite film is proven to be relatively general, confirmed by several widely used large cation organic salts (BAI, PEAI, and PEABr). The corresponding solar cells with oriented perovskite films exhibit a significantly reduced V_{OC} loss (by 70 mV), much larger EL quantum efficiency (ELQE) by one order of magnitude, enhanced PCE up to 23.15%, and significantly boosted stability which maintained 95% of initial PCE after 2600h ambient storage without encapsulation.

Results

Two types of perovskites were investigated and prepared by the conventional two-step method: Type 1 - The so-called FAMA perovskite with the composition of $(FAPbI_3)_{1-x}(MAPbBr_3)_x$ was fabricated through depositing organic salts (FAI, MABr) precursor onto prepared PbI_2 film, followed by an annealing process (**Figure 1A**). Type 2: Large alkylammonium cation n-butylammonium bromide (BABr) was dissolved in the precursor of organic salts to prepare the so-called BAFAMA perovskite. The detailed experiment method was shown in the experiment section. For each type of the perovskites, samples with and without MACl was also compared to study the crystal properties. The grazing-incidence wide-angle X-ray scattering (GIWAXS) measurements were conducted to investigate the crystallographic structure of the perovskite films with and without BABr (BABr: FAI = 4%). The corresponding polar intensity profiles integrated along the (100) ring were shown in **Figure 1D and 1H**, and the polar angle (χ) stands for the angle to the substrate normal. For FAMA perovskite films, from the GIWAXS patterns and the corresponding polar intensity profiles, no preferential orientation was found for both samples regardless of the addition of MACl, as shown in **Figure 1D**. Nevertheless, the incorporation of MACl in FAMA perovskites will induce the formation of the PbI_2 phase at $q = 0.9$ Å^{-1} and suppress the perovskite phase (**Figure 1C and 1E**). A similar phenomenon was observed in the BAFAMA perovskites as well (**Figure 1G and 1I**). The emergency of the PbI_2 peak could be attributed to the coordination of MACl with PbI_2 and formed intermediate phase which prevents the fast reaction and uncontrollable reaction between PbI_2 and organic molecules such as FAI and MABr [14]. Besides, the BAFAMA perovskite film without MACl also exhibited randomly oriented crystals with a weak preferential orientation, in the light of the weak peak centered at 55º from the polar intensity profiles in **Figure 1F and** 1**H**.

The addition of MACl in the BAFAMA perovskite film was found to greatly strengthen the peak at 55º, indicating a strongly enhanced crystal orientation achieved with the aid of MACl (**Figure 1G and 1H**). From the intensity profiles in **Figure 1E and 1I**, the diffraction peaks position of (100), (200) and other characteristic peaks remained unchanged, indicating the additive of MACl was not incorporated into the perovskite lattice and released during the annealing process. These results indicated MACl accompanied by BABr could effectively regulate the orientation of perovskite film via the benchmark two-step method.

The synergetic effect was also observed for other long-chain organic salts (BAI, PEAI, and PEABr), shown in figure. S1. The GIWAXS maps presented the high orientation of perovskite via the synergy of long-chain organic cation and MACl. In the cases of solely long-chain organic salts (w/o MACl), or solely MACl, the same two-step process

gave isotropic perovskite film orientation.

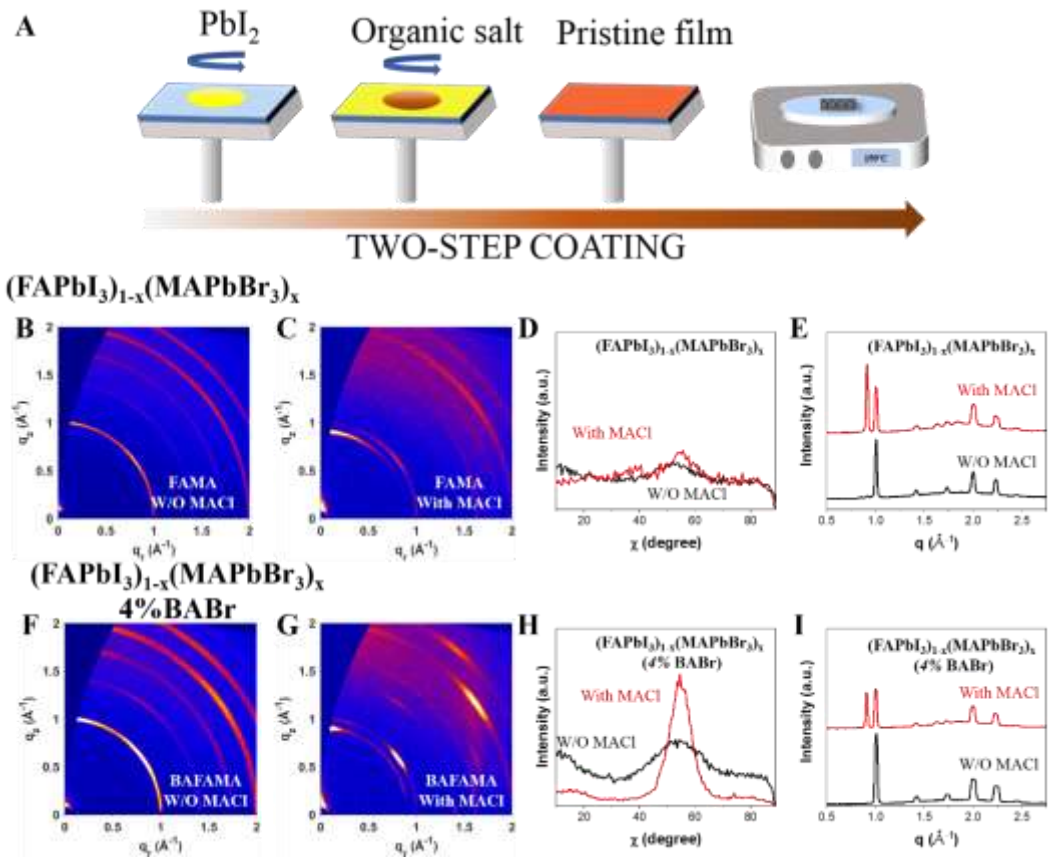

Figure 1. Perovskite film processing and synergetic effect of MACl and BABr on the perovskite crystal orientation. (A) Schematic of the fabrication process via a two-step method. The GIWAXS characterization for two different perovskite types: (B) FAMA perovskite (w/o MACl), (C) FAMA perovskite (with MACl), (F) BAFAMA perovskite (w/o MACl), and (G) BAFAMA perovskite (with MACl). The polar intensity profiles along the ring at the range of 0.95-1.05 $Å^{-1}$ for (D) FAMA and (H) BAFAMA perovskite. The polar intensity profiles averaged along with the rings corresponding for (E) FAMA and (I) BAFAMA perovskite.

To elucidate the mysterious origin of the crystal orientation, we investigated the crystallization kinetics in the two stages of the perovskite growth process: (1) the formation of the intermediate phase right after the second step organic salts precursor coating, and (2) the perovskite crystallization during the annealing process.

To reveal this intermediate phase formation process, *in situ* GIWAXS measurements (2°) were conducted on FAMA and BAFAMA perovskite films, all with MACl. The GIWAXS intensity profiles and the corresponding false-color intensity maps versus *q* and frames for perovskites without and with BABr were summarized in **Figure 2**. For the perovskite without BABr, it exhibited a typical phase transition process from PbI_2 to perovskite intermediate phases including three crystallization stages. At stage I, only the peak of PbI_2 at q = 0.9 $Å^{-1}$ and FTO substrate signal at q ≈ 1.9 $Å^{-1}$ were observed. Stage II was then triggered by the dropping of organic salts, as

indicated by a broad peak centered at q ≈ 1.45 $Å^{-1}$ in GIWAXS profiles, giving rise to the phase transition from PbI_2 to perovskite intermediates. Therefore, the peak intensity of PbI_2 was quickly decreased while the perovskite peak at q ≈ 1.0 $Å^{-1}$ was built up in seconds. During this process, a dissolution-crystallization process was proposed to initiate the transformation from pristine film to the perovskite intermediate phase [15]. It is reported that the solution with a higher concentration of I^- ion favored the formation of PbI_4^{2-} and PbI_3^- which were dissolved in the IPA [16]. For FAI based organic salts precursor with an excess amount of I^{-1} ion, the initially formed Perovskite crystal and PbI_2 on the film surface reacted with I^{-1} ion by the following reactions:

$$CH(NH_2)_2PbI_3(s) + xI^-(sol) \rightarrow CH(NH_2)_2^+(sol) + PbI_{2+x}^{x-}(sol) \quad (1)$$

$$PbI_2(s) + xI^-(sol) \rightarrow PbI_{2+x}^{x-}(sol) \quad (2)$$

After the precursor was oversaturated with PbI_4^{2-} or PbI_3^- complexes, the PbI_{2+x}^{2-} or PbI_2 reacted with FA^+ or MA^+ ions and the nucleation of small perovskite grains will start. The chemical reactions were expressed as:

$$PbI_{2+X}^{X-}(sol) + CH(NH_2)_2^+ \rightarrow CH(NH_2)_2PbI_3(s) + xI^-(sol) \quad (3)$$

$$PbI_2(s) + CH(NH_2)_2^+(sol) + I^-(sol) \rightarrow \quad CH(NH_2)_2PbI_3(s) \quad (4)$$

For the perovskite film with MACl, since MACl could effectively slow down the nucleation process by controlling the delivery speed of PbI_2 [17], it could prevent the fast and uncontrollable reaction between PbI_2, FAI, and BABr expressed as:

$$PbI_2 + FAI + xMACl \rightarrow FAI \cdot PbI_2 \cdot xMACl \quad (5)$$

After entering stage III, the formation of the perovskite intermediate phase continued and the residual unreacted PbI_2 phase left. The addition of Br^- also play an important role, the incorporation of Br could accelerate the formation of perovskite crystals and lead to a direct phase transition from precursor to perovskite[18] rather than via intermediate phases in the pure iodide perovskite film. In addition, Cl ions may slow down the perovskite crystallization process due to the formation of solvated phases[17b].

The perovskite with BABr, however, experienced four crystallization stages during the formation of perovskite crystallites. The first three stages were similar to the perovskite without BABr, but an additional stage IV was observed in the *in situ* GIWAXS profiles (**Figure 2E and 2F**). After the formation of the perovskite phase in stage III, two peaks at q = 0.79 and 1.09 $Å^{-1}$ arose at ≈ 30 s of the spin coating, indicating the beginning of stage IV. These two peaks as well as the perovskite peak were further enhanced and then saturated at stage IV, accompanied by the decrease of the PbI_2 peak. It is noted that these two peaks at q = 0.79 and 1.09 $Å^{-1}$ likely came from the BA-related phase, as indicated by the XRD pattern of PbI_2-BABr intermediate film (figure. S2A). The additional stage of large organic cation related phases was also reported in the one-step method [19]. *In situ* GIWAXS with two incident angles (1° and 2°) were summarized in

figure. S3 to investigate the position of the BA-related phase within the film. The thickness of the intermediate phase film was around 730nm verified through cross-section SEM (figure. S2B). For the incident angle of 1°, the beamline can only penetrate around 700nm of the intermediate film. From the GIWAXS intensity profiles of 1°, the signal of two BA-related phases was very weak, indicating the BA-related phase was dominantly located at deeper than 700nm below the top surface (figure. S3, B and C). Temporally, the formation of BA-related phases in 1° case happened later than in the 2° case (by ~30s), which could be attributed to the lower Gibbs free energy at the bottom interface[20]. From the last frame of in situ GIWAXS mapping, we find the perovskite phase and BA-related phase are consistent, i.e. both have strong orientations at ~55° (figure. S4). It is worth mentioning that the crystal orientations of the perovskite phase and BA-related phase are consistent, i.e. both have strong orientations at ~55° (figure. S4 B). In addition, the peak positions of the perovskite (100) plane and the BA-related phase are 1.01 $Å^{-1}$ and 1.08 $Å^{-1}$ (figure. S4C), corresponding to the d-spacing values of 6.22 Å and 5.82 Å, respectively. It is reported that halide perovskites possess a "soft crystal lattice, allowing greater tolerance to lattice mismatch"[12a]. Therefore, it is possible for the epitaxial growth of the perovskite crystals based on the BA-relates phase with a small lattice mismatch.

The (100) phase orientations of the two perovskite intermediate films (with MACl) – Control vs. with BABr - were exhibited in figure. S2 (D and E). Both intermediate films exhibited a preferred 55° orientation. Interestingly, the intermediate crystalline phases with BABr did not exhibit a better orientation compared with the film without BABr. We suspected the preferred 55° orientation of perovskite film via the two-step method was determined at the first stage during the reaction of organic salts with PbI_2. The generation of BA-related intermediate phases was after the formation of the normal perovskite intermediate phase. The BA-related intermediate phase, therefore, has a very limited effect on the orientation of the intermediate phase. Therefore, the difference in the crystal orientation of well-formed FAMA and BAFAMA perovskite should be originated from the annealing/conversion process of perovskite.

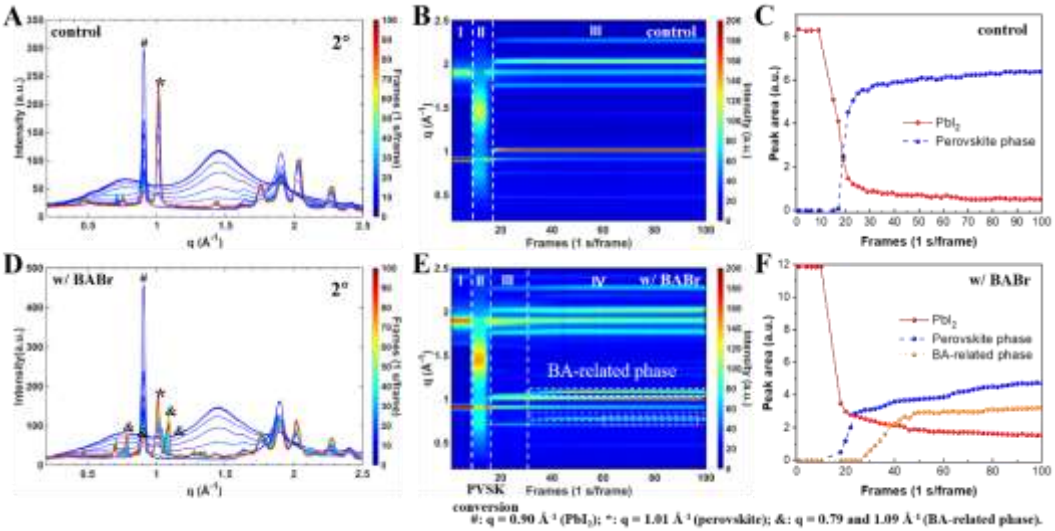

Figure 2. Time-resolved GIWAXS profile analysis - the formation of intermediate perovskite films. GIWAXS intensity profiles for the perovskite films (A) without and (D) with BABr, (B, E) the corresponding false-color intensity maps versus *q* and frame numbers, and the time evolution of peak areas of (C) without and (F) with BABr. #, *, and & denote the PbI_2 phase, perovskite phase, and BA-related phase.

The intermediate phase film would convert into complete perovskite film (~ 450 nm) through the annealing process. A thorough investigation of the crystallography structure was conducted on the complete perovskite films with different BABr concentrations (0%, 4%, and 8%). The depth-resolved crystallography characterization was conducted by changing the incident angles of GIWAXS measurement[21]. Three angles were selected: 0.1°, 0.3°, and 1° (**Figure 3)**. For the incident angle below the critical angle ($\alpha < 0.2°$), the x-ray source can only penetrate the top 10 nm of the perovskite film. For the incident angle $0.2 < \alpha < 0.4°$, the GIWAXS map exhibits the information of the bulk/middle layer of perovskite film. For the incident angle of 1°, the x-ray beam would penetrate the whole 450 nm perovskite film. From the GIWAXS patterns, the rings around q_z of 1, 2, and 2.5 $Å^{-1}$ were corresponded with (100), (200), and (210) diffraction peaks. Continuous Debye-Scherrer rings with homogenous intensity over q_r of 1 and 2 $Å^{-1}$ were observed from all three incident angles of FAMA perovskite GIWAX maps, indicating an isotropic orientation of perovskite crystallites for FAMA perovskite at different film depth. For the BAFAMA perovskite, however, Bragg spots along the rings of q_z of 1 and 2 A^{-1} were observed from all three incident angles, indicating the incorporating of BABr induced the oriented growth of BAFAMA perovskite throughout the film. The intensity of the scattering as a function of azimuthal angle over the (100) phase was exhibited in figure. S5 (A-C), showing the BAFAMA perovskite has a strong orientation at 55° over the FAMA perovskite film.

The corresponding polar intensity profiles averaged along the rings were shown in figure. S5 (D-F). The diffraction peaks at 0.9, 1.0, 2.0, and 2.5 were corresponding with PbI_2, (100), (200), and (210) of the perovskite crystal plane, respectively. The intensity ratio of PbI_2/perovskite (100) phase was calculated from polar intensity profiles (**Figure**

3D, 3F, and 3H). The ratio of PbI_2/perovskite (100) gradually increased from the bottom (1°) to the top surface (0.1°), indicating a higher residual PbI_2 on the surface. The different ratios of PbI_2/perovskite (100) were attributed to the reaction sequence - the layer with a lower ratio was formed earlier than the film with a higher ratio. Therefore, the formation of the bottom layer perovskite was earlier than the top surface perovskite, i.e., the growth of perovskite was a bottom-up process. This could be due to the thermal transfer sequence that the heat transfer from the glass side to the top perovskite.

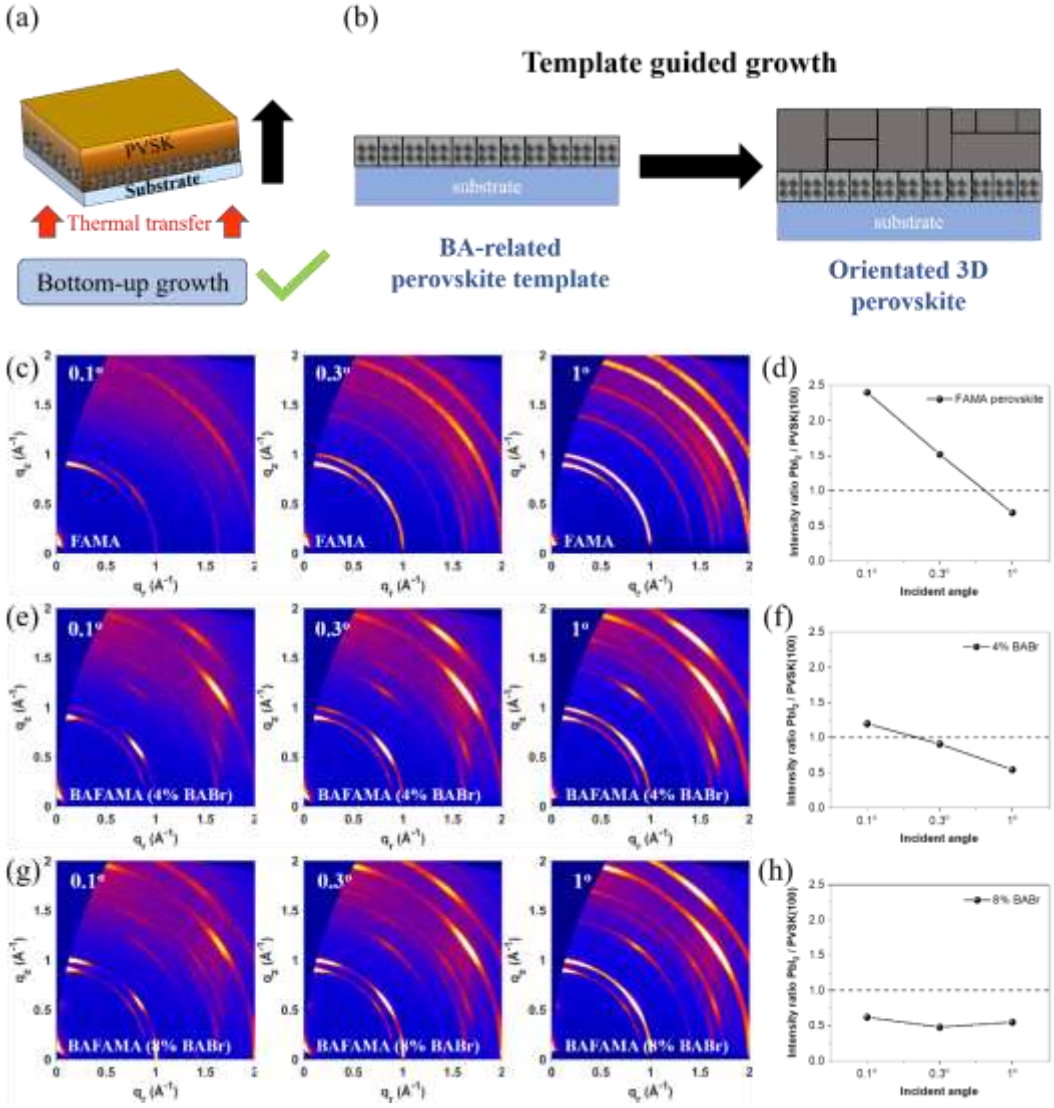

Figure 3. Template-guided growth of perovskite film from the intermediate phase. (A) Bottom-up growth of perovskite via a two-step method. (B) Schematic of template-guided growth of perovskite film during the annealing process. The GIWAXS maps of (C) FAMA perovskite, (E) BAFAMA (4% BABr) perovskite, and (G) BAFAMA (8% BABr) perovskite with different incident angles. The PbI_2/PVSK (100) phase intensity ratio with different incident angles for (D) FAMA perovskite, (F) BAFAMA (4% BABr) perovskite, and (H) BAFAMA (8% BABr) perovskite.

To double-check the hypothesis, we compared the perovskite films annealed from the top film surface (top-annealed perovskite) and the glass side. To analyze the distribution of PbI_2 over various depths of perovskite film, GIWAXS (with incident angles of 0.1^o, $0.3^{o,}$ and 1^o) measurements were conducted onto the top-annealed BAFAMA and FAMA perovskite film (**Figure 4**). From the GIWAXS results, no PbI_2 signal was found from the top layer (0.1^o) of two top-annealed perovskite films (**Figure 4A**, **4D** and **4G**). However, a clear Bragg spot along the rings of 0.9 $Å^{-1}$ (PbI_2) was found from the GIWAXS maps of 0.3^o and 1^o, indicating residual PbI_2 was precipitated in the middle and bottom sections of films annealed from the perovskite top side. From SEM images of FAMA perovskite films annealed from two different sides, we did not find any residual PbI_2 on the SEM image of the film annealed starting from the top surface (figure. S6), while clear white areas (residual PbI_2) were observed on the grain edges of the film annealed from the glass side (figure. S7A). These results were consistent with our previous assumption that the thermal transfer sequence can determine the growth pattern of the perovskite film (bottom-up or top-down). Additionally, the orientation of perovskite crystal annealed from the different sides were compared (**Figure 4I)**. It is noteworthy that two BAFAMA films exhibited distinct crystallographic property that the top-annealed BAFAMA film exhibited poor orientation similar to FAMA films.

Therefore, the BA-related intermediate phase on the bottom layer played a critical role in the perovskite crystal orientation during the annealing process. For the glass side annealed BAFAMA perovskite film, the first formed oriented template could lead to an ordered growth of subsequent perovskite layer (**Figure 3B**). On the contrary, for the top annealed film, as no BA-related intermediate phase on the top surface as a template, the whole film exhibited poor orientation.

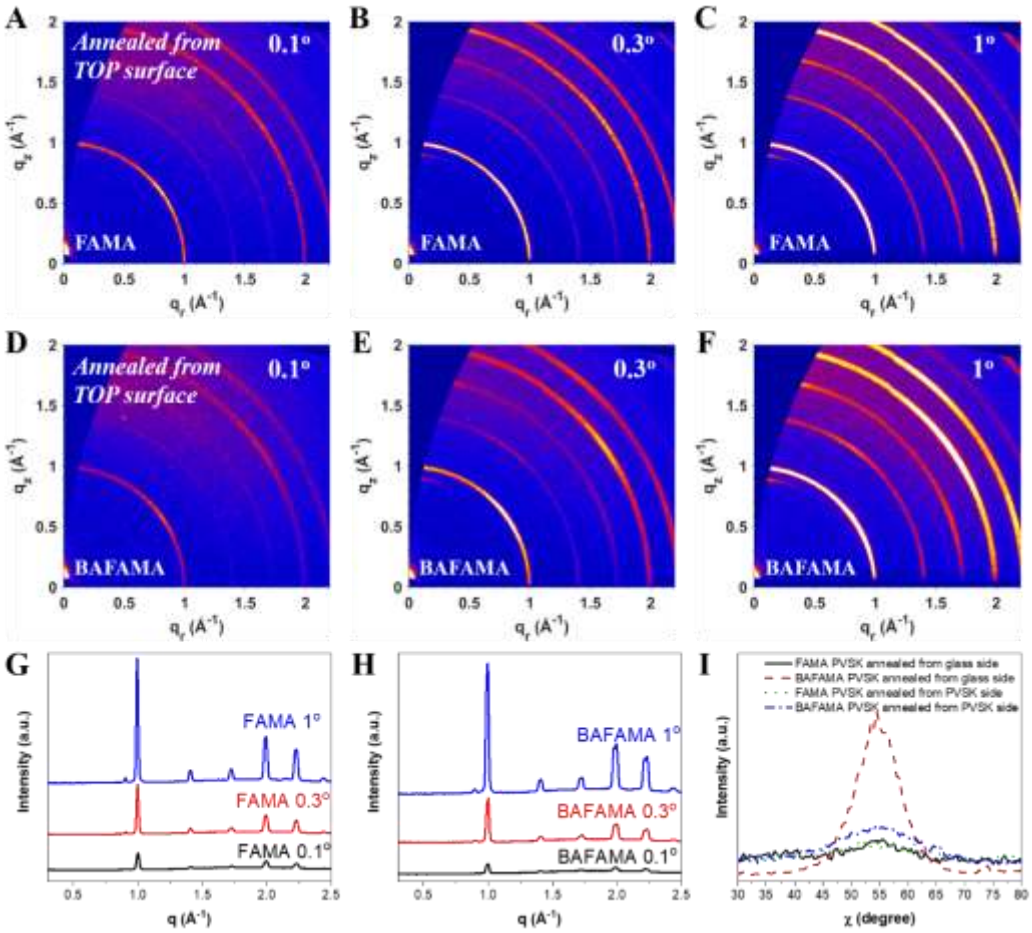

Figure 4. The crystallographic characterization of perovskite film annealed from the top surface. The GIWAXS maps for (A-C) FAMA and (D-F) BAFAMA film annealed from the top perovskite intermediate surface. The polar intensity profiles averaged along the rings corresponding for three different incident angles (0.1°, 0.3°, and 1°) of (G) FAMA perovskite and (H) BAFAMA perovskite. (I) The corresponding polar intensity profiles over azimuthal angle extracted from the ring at the range of 0.95-1.05 $Å^{-1}$ for perovskite annealed from the glass side and perovskite top surface side.

Furthermore, the distribution of the BA-related phase inside highly oriented perovskite film was further verified through the photoluminescence (PL) measurement incident from the glass side and air side (figure. S8). A clear blue shift was observed from BAFAMA perovskite film PL when illuminated from the glass side, comparing to the airside incidence. This is especially true for the film incorporating 8% BABr, which was attributed to a higher bandgap of perovskite with rich BABr at the bottom. The distribution of BA-related perovskite was consistent with the results of the *in situ* GIWAXS measurements of the intermediate phase, i.e., mainly at the bottom layer.

To demonstrate the influence of the first-formed bottom layer on the following perovskite growth, we mimicked this by utilizing different substrates: amorphous glass and single crystalline silicon (100). We compared the crystallinity and crystal orientation of perovskite film grown on glass and silicon (figure. S9). The perovskite

film coated on the glass substrate exhibited an isotropic ring of (100) plane despite a weak peak centered at χ = 55°, implying that the perovskite crystals on the glass substrate are almost randomly oriented, with only a weak preferential orientation (figure. S9C). By contrast, the peak centered at χ = 55° is much enhanced for the film-coated on the Si (100) substrate, suggesting the critical role of the bottom substrate on the growth of perovskite film, considering the soft lattice constant of the material [12a]. This further confirms that the significant influence of the bottom layer/substrate on the subsequent growth of the perovskite layer.

Based on these results, we proposed a bottom-up quasi-epitaxial growth model to explain the crystallization kinetics of the perovskite film via a two-step method (**Figure 5**). To achieve the quasi-epitaxial growth, the growth process must be slow enough to enable an atomic level self-assemble over the template. In our case, this can be achieved by MACl which could effectively regulate the growth speed. The BA-related intermediate phase was preferable to be located at the bottom of the intermediate film and naturally served as the growth template in the thermal annealing process. Remarkably, we revealed and proved a bottom-up growth of perovskite thin film which was extremely important for the template guided quasi-epitaxial growth. The bottom BA-related intermediate phase was first converted into an oriented perovskite template. The oriented bottom template then leads to a quasi-epitaxial growth of perovskite with strong orientation. Without either BABr or MACl, an oriented perovskite template cannot be formed, and it would cause a random growth of perovskite. The poor orientation of top-annealed BAFAMA film was also consistent with this scenario as BA-related intermediate phases are located at the bottom rather than the top, thus no template formation.

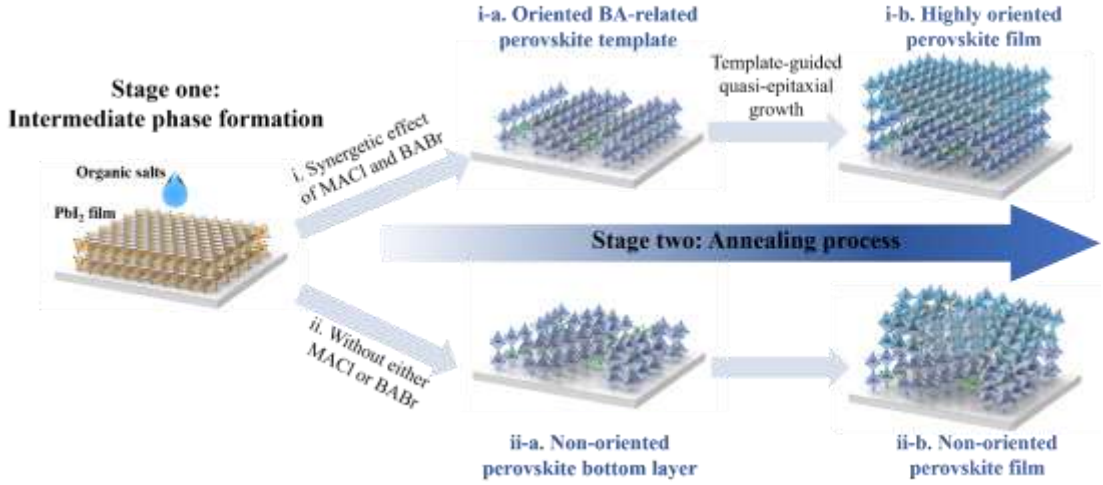

Figure 5. Schematic illustration of the bottom-up quasi-epitaxial growth of hybrid perovskite via a two-step method. i. With both MACl and large cation salt, i-a. the growth of bottom BA-related perovskite template on the substrate, i-b. highly oriented film; and ii. missing either MACl or large cation salt or both, ii-a. the non-oriented bottom layer, ii-b. non-oriented perovskite film.

To investigate the photovoltaic properties of the BAFAMA perovskite via bottom-up quasi-epitaxial growth, the perovskite solar cells of FAMA perovskite and BAFAMA

perovskite incorporating with 4 mol%, 8 mol%, and 12 mol% of BABr were prepared via a two-step method with MACl assistant (see the materials and methods section). The device structure of the perovskite solar cells was ITO/SnO_2/perovskite/spiro-OMeTAD/Au. The current density-voltage (J-V) characteristics of devices (active area: 0.04 cm^2) with different BABr concentrations were shown in **Figure 6A**, where the parameters were tabulated in **Table 1**, and the external quantum efficiency was shown in **Figure 6B**. The best PSC performance was achieved by incorporating 4 mol% of BABr. The corresponding PCE was 22.7%, with a short-circuit current density (J_{SC}) of 24.4 mA cm^{-2}, a fill factor (FF) of 79%, and an open-circuit voltage (V_{OC}) of 1.18 V. The reference FAMA perovskite device exhibited a PCE of 20.7%, with a short-circuit current (J_{SC}) of 23.9 mA cm^{-2}, a fill factor (FF) of 78%, and an open-circuit voltage (V_{OC}) of 1.11 V. For a higher concentration of BABr, the performance of devices was reduced where the current density was dropped from 24.4 mA/cm^2 (4% BABr) to 22.9 mA/cm^2 (8% BABr) and 20.3 mA/cm^2 (12% BABr), which is attributed to the fact that the higher concentration of BABr would block the carrier transportation. In comparison with the reference FAMA perovskite device, the V_{OC} was increased from 1.11 V to 1.18 V and J_{SC} was enhanced from 23.9 mA/cm^2 to 24.4 mA/cm^2 for the perovskite with 4% BABr. The great enhancement in the open-circuit voltage could be attributed to the reduced defects and high crystallinity of the film by quasi-epitaxial growth. With the anti-reflection (AR) coating, the J_{SC} of the BAFAMA device was further enhanced from 24.4 mA/cm^2 to 25 mA/cm^2 and we obtained a PCE of 23.15% (figure. S10E). For the large area device (0.8 cm^2), the template guided growth device (BAFAMA perovskite) exhibits a PCE of 21.2% with the Voc of 1.16 V, Jsc of 23.7 mA/cm^2, and FF of 0.77 (figure. S11). While for the control device (FAMA perovskite), it exhibits Voc of 1.08 V, Jsc of 23.0 mA/cm^2, and FF of 0.73 which contributes the PCE of 18.1%. The large area BAFAMA device also conforms to a better performance than the control device, which indicated our proposed mechanisms work well on larger area cases. From the EQE spectra, the bandgaps of perovskite films were calculated as follows: 1.55eV for FAMA perovskite and BAFAMA perovskite with 4% BABr, 1.56eV for perovskite with 8% BABr, and 1.58 eV for perovskite with 12% BABr. The integrated J_{SC} values from EQE spectra for these devices were in good agreement with the values from J-V curves (within 5% deviation). An obvious blue shift was found in the absorption of perovskite films with the increasing concentration of BABr, which was consistent with the EQE results (**Figure 6B and 6C**). The BAFAMA perovskite solar cell with 4% BABr has also achieved a steady power output of 22.3% PCE with almost no hysteresis (**Figure 6D and 6E**). The statistic distribution of the photovoltaic parameters was shown in figure. S10 (A-D) for the FAMA perovskite and BAFAMA perovskite with 4% BABr, collected from 20 solar cells for each type.

The origin of enhanced open-circuit voltage (V_{OC}) was characterized through the reciprocity principle via electroluminescence techniques [22]. The open-circuit voltage of the ideal solar cell can be calculated from the classic equation: $V_{oc} = \frac{K_B T}{q} \ln \frac{J_{SC}}{J_0}$. Here, q is element charge, K_B is Boltzmann constant, T is temperature, J_{SC} is the short circuit current density and J_0 is the recombination current density or dark current density. The

J_{SC} was calculated through an overlap integral between EQE_{PV} and solar photon flux[23]: $J_{SC} = q\int_0^\infty EQE_{PV}(\lambda)\cdot \emptyset_{AM1.5}(\lambda)d\lambda$. For real cell, J_0 was the sum of radiative and non-radiative recombination currents. In equilibrium, the radiative recombination current equal with emitted photon current. Therefore, $J_{0,rad}$ can be calculated through the following equation: $J_{0,rad} = q\int_0^\infty \emptyset_{BB}(\lambda)\cdot EQE_{PV}(\lambda)\cdot d\lambda$. The non-radiative recombination current could be calculated through external electroluminescence quantum efficiency: $EQE_{EL} = \frac{J_{0,rad}}{J_{0,rad}+J_{0,non-rad}}$. According to the reciprocity principle [22], the open-circuit voltage was obtained : $V_{OC} = V_{OC}^{rad} + \frac{kT}{q}\ln(EQE_{EL})$. For the EL measurement, both of FAMA and BAFAMA perovskite solar cells were operating as LED in (**Figure 6F**). The emission peak of BAFAMA perovskite was located at 796nm. The EQE_{EL} of FAMA perovskite was 0.2% with the injection current of 23.9 mA/cm^2, while BAFAMA perovskite exhibited a boosted EQE_{EL} of 5.6% under injection current of 24.4 mA/cm^2. The calculated V_{OC} loss from non-radiative recombination were 159 mV and 74 mV for FAMA perovskite and BAFAMA perovskite, respectively. The low non-radiative recombination loss for the BAFAMA perovskite was ascribed to the low defects level of perovskite film via ordered quasi-epitaxial growth.

Moreover, steady-state photoluminescence (PL) and time-resolved photoluminescence (TRPL) spectroscopy measurements were conducted on samples of FAMA perovskite and BAFAMA perovskite to characterize the carrier dynamics (**Figure 6G and 6H**). From **Figure 6G**, we found the PL intensity was enhanced by around 200% for the film with 4% BABr, and around 100% for the film with 8% BABr which indicated the great suppression of nonradiative recombination for the incorporating of BABr, indicating fewer defects in the quasi-epitaxial grown perovskite guided by an oriented bottom template. The reduced PL intensity of the film with 8% BABr might be due to the low fluorescence with a higher concentration of BA-based perovskite.

The TRPL spectroscopy of perovskite with different concentrations of BABr was shown in **Figure 6H**. The TRPL curves were analyzed by performing curve-fitting to the exponential equation ($I = I_1 e^{-t/\tau_1} + I_2 e^{-t/\tau_2}$) and extracted the associated lifetime τ_1 and τ_2. The τ_1 decay component was related to non-radiative recombination from defects, and τ_2 component corresponded with the radiative recombination from the bulk perovskite. The FAMA perovskite presented the characteristic PL lifetime of τ_1 of 36.5 ns and τ_2 of 206.2 ns. The TRPL decays exhibited longer lifetimes and fewer dispersion rates with τ_1 of 140 ns and τ_2 of 1025 ns for the film of 4% BABr, and τ_1 of 200 ns and τ_2 of 850 ns for the film of 8% BABr. The TRPL measurement results further proved the quasi-epitaxial growth of perovskite can greatly enhance the optoelectronic performance with effectively suppressed nonradiative recombination. The x-ray diffraction pattern for the pure BABr film, FAMA perovskite film, and

BAFAMA perovskite films were shown in **Figure 6I**. The diffraction pattern for the samples displayed 5 dominant peaks which located at 12.7° corresponding to the PbI_2 phase and 14.1°, 24.3°, and 28.1° corresponding to (100), (110), and (200) of perovskite crystal planes respectively [24]. From the XRD pattern, no characteristic diffraction peak of BABr was found in the patterns of BAFAMA perovskite because the majority of BABr was converted to the perovskite phase. As shown in the XRD pattern, excess of PbI_2 was used to passivate the defects in the perovskite film and improve device efficiency[25]. For the film without BABr, the excess PbI_2 mainly locates at the top surface of the film, as proved in Figure 3C and 3D. In contrast, the addition of BABr can result in a uniform distribution of the excess PbI_2 among the film (Figure 3E-H), passivating defects at grain boundaries. Also, we found the intensity of the PbI_2 peak was reduced for the BAFAMA perovskite, especially for the perovskite with 8% concentration of BABr. This could be owing to the reaction of BA-related perovskite that would lead to a reduction of PbI_2 content. The PbI_2 phase will experience a different structural evolution for a one-step process. It is noted that the two-step process consisits of the sequential deposition of a PbI_2 layer (step 1) and organic salts (step 2), so the PbI_2 signal will undergo a significant drop during the second step because of the formation of perovskites after the interdiffusion between PbI_2 and organic salts, as shown in Figure 2. In comparison, for the one-step process, the formation of the PbI_2 phase is mainly from the decomposition of perovskite crystals during the annealing[21a]. The origins of PbI_2 in the two-step process and one-step process are therefore different.

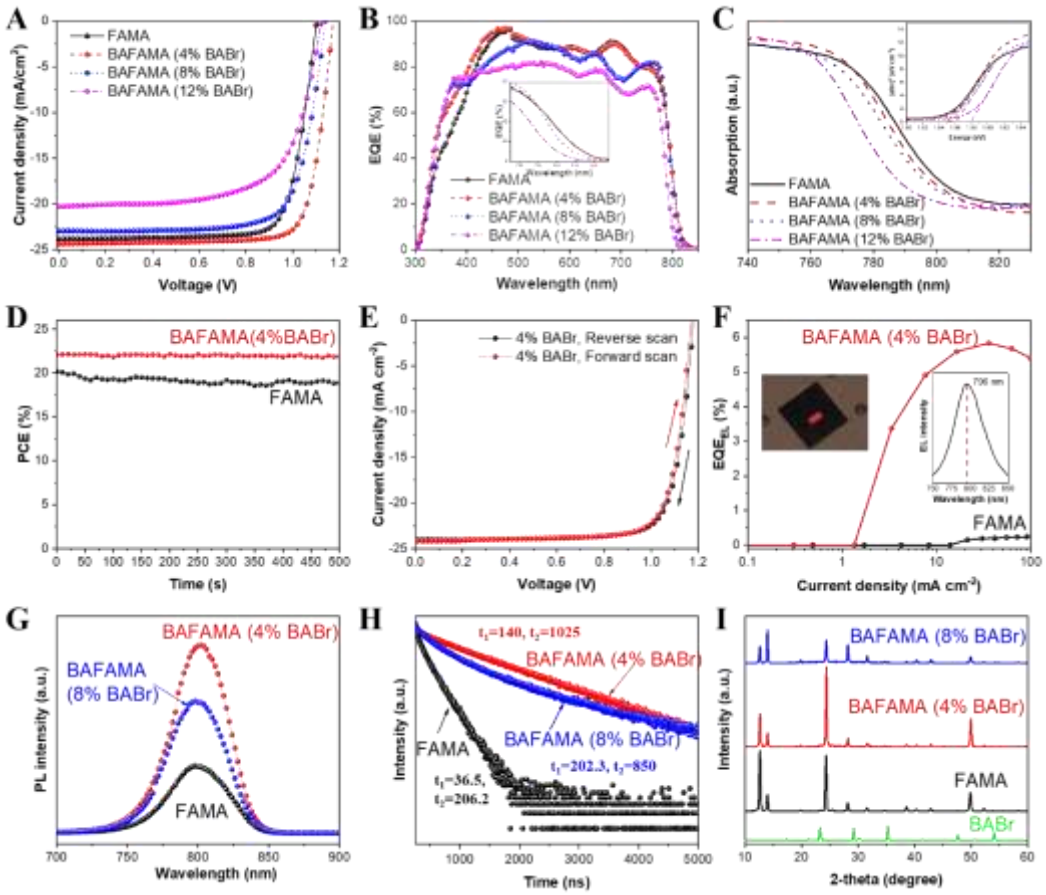

Figure 6. Photovoltaic and optoelectronic properties of FAMA perovskite and BAFAMA perovskite via quasi-epitaxial growth. (A) J-V curves for the perovskite solar cell with different concentration of BABr; (B) Corresponding External quantum efficiency (EQE) spectra of these cells; (C) Absorption of FAMA and BAFAMA perovskite films; (D) Steady-state output at the maximum power point of FAMA perovskite solar cell and BAFAMA perovskite solar cell with 4% BABr; (E) J-V curves of forward and reverse scan for BAFAMA perovskite with 4% BABr; (F) EQE_{EL} and EL spectrum of perovskite; (G) Steady-state photoluminescence spectrum of perovskite films; (H) Time-resolved photoluminescence decay spectra of corresponding perovskite films; (I) XRD patterns of corresponding films.

Table 1. Photovoltaic parameters of the champion cell for FAMA perovskite device and devices with BABr of different concentrations, under simulated AM 1.5G irradiation at 100 mW cm^{-2}.

Device	V_{OC} [a)] (V)	J_{SC} [a)] (mA cm^{-2})	calc. J_{SC} [b)] (mA cm^{-2})	FF [a)] (%)	PCE[a)] (%)
FAMA perovskite	1.11	23.9	23.01	78	20.7
BAFAMA perovskite (4% BABr)	1.18	24.4	23.33	79	22.7
BAFAMA perovskite (8% BABr)	1.14	22.9	22.15	74	19.3
BAFAMA perovskite (12% BABr)	1.12	20.3	19.92	67	15.2

[a)] Values are for the highest-PCE device. [b)] J_{SC} value from the integration of the EQE spectra is within 4% error of those from *J-V* curves.

The morphology of FAMA perovskite and BAFAMA perovskite films with different concentrations of BABr was studied through scan emission microscope (SEM) and atomic force microscope (AFM). From the SEM image, the BAFAMA perovskite exhibited a similar morphology with the FAMA perovskite, for example, similar grain size and existence of PbI_2 on the grain edges (figure. S7, A-D). This is supported by our proposed quasi-epitaxial growth model that the bottom perovskite template could affect the assembling of perovskite crystal such as phase orientation and crystallinity and while had little effect on the nuclei formation of perovskite.

The AFM images of perovskite films were shown in figure. S7 (E-H). The AFM images exhibited similar results with SEM images. For the FAMA perovskite film, the surface average roughness (R_a) was around 28 nm and the root mean square roughness (R_q) was around 35.6 nm. The BAFAMA perovskite film (4% BABr) shown a lower roughness where the surface average roughness (R_a) was around 26.5 nm and the root

mean square roughness (R_q) was around 33.1 nm. With a higher concentration of BABr, the roughness of perovskite film was enhanced. For the BAFAMA perovskite film (8% BABr), the surface average roughness (R_a) was around 27.5 nm and the root mean square roughness (R_q) was around 34.3 nm. And the surface average roughness (R_a) for 12% BABr BAFAMA perovskite film was around 28.2 nm and the root mean square roughness (R_q) was around 35.3 nm. The incorporation of 4% BABr could greatly reduce the surface roughness of perovskite film which was due to the ordered growth of perovskite film.

At present, the stability of the perovskite solar cell is the most challenging issue toward commercialization. The BAFAMA perovskite exhibited an enhanced hydrophobicity over FAMA perovskite, which is in good agreement with other large organic cations/2D-materials[10i, 11, 26]. The static contact angles of deionized water on the top of FAMA perovskite, BAFAMA perovskite (4%, 8%, and 12% BABr) films were 10.1°, 15.1°, 17.5°, and 32.5°, respectively (figure. S12A). Stability tests were conducted onto the FAMA perovskite and BAFAMA perovskite with 4% BABr including storage stability and photo-stability (figure. S12, B and C). For storage stability, the non-encapsulated devices were kept in a dry box with the humidity of 15 to 20% under dark for 2600 h. The non-encapsulated BAFAMA perovskite device maintained 95% of its initial PCE after 2600 h, while the control FAMA perovskite device only maintained 75% of its initial PCE (figure. S12B). The photostability was measured by exposing the encapsulated FAMA and BAFAMA perovskite devices to a white light-emitting diode array with equivalent 0.8 suns AM 1.5G. The encapsulated BAFAMA perovskite maintained 80% of its initial PCE after 600h illumination, while the control FAMA perovskite device only has 20% of its initial PCE (figure. S12C). The t_{80} lifetime of both devices was also exhibited in figure. S10C - 600 h for BAFAMA perovskite, which was over 4 times longer than the t_{80} lifetime of FAMA perovskite (130 h).

Conclusion

In this work, we reported a facile and universal bottom-up quasi-epitaxial growth of highly oriented α-$FAPbI_3$ perovskite via a two-step solution process method. In-depth GIWAXS characterizations systematically illuminated the synergetic effect of MACl and large-organic cations (e.g., BABr, BAI, PEAI, and PEABr) on the crystallization kinetics and precise crystallographic orientation control. The *in situ* formation of the BA-related intermediate phase was found to be at the film bottom for the first time, which resulted in an oriented template for the followed perovskite bottom-up quasi-epitaxial growth during thermal annealing. The novel solution process bottom-up quasi-epitaxial perovskite growth presented a significant advance in understanding the growth kinetics of perovskite.

It worth noting that this investigation is on α-$FAPbI_3$ perovskite for proof of concept, and the understanding of solution-processed quasi-epitaxial perovskite growth is just a beginning. Future deepened study (for example, visualizing *in situ* epitaxial growth process), and the validation of the technique in broader perovskite systems are strongly needed for the quasi-epitaxial grown perovskite concept to be applied. Other approaches to achieve quasi-epitaxial grown perovskite films will also be very

important for the future development of high-performance perovskite optoelectronic devices in large, not limited to solar cells.

Acknowledgements: All authors are grateful for the beamtime and technical support provided by 23A SWAXS beamline at NSRRC, Hsinchu.

Funding:

G.L. would like to thank the support by Research Grants Council of Hong Kong (Grant No. 15246816, and C5037-18G), Shenzhen Science and Technology Innovation Commission (Project No. JCYJ20170413154602102), the Project of Strategic Importance (Project No. 1-ZE29), University Supporting Fund for Major Research (1-BBAS) and Sir Sze-yuen Chung Endowed Professorship Fund (8-8480) provided by the Hong Kong Polytechnic University; X. Lu and M. Qin acknowledge the financial support from Research Grant Council of Hong Kong (GRF No. 24306318).

Author contributions:

H.Z. and M.Q. contributed equally to this work. G.L. and H.Z. conceived the paper. H.Z. and Z.C. conducted the fabrication of perovskite films and perovskite solar cells. M.Q and X.L. performed *in situ* and *ex situ* GIWAXS and analyzed the data. Z.R., K.L., Q.L., J.H., and W.Y. assisted in the characterization of SEM, XRD, AFM, EL, and PL measurements. Y.Z. and Z.Z measured contact angles and optical transmission. P.W.K.F. provided the technical support in lab equipment. H.Z., M.Q., X.L., and G.L. wrote the manuscript. G.L. and X.L. supervised this work.

Competing financial interests:

The authors declare no competing financial interests.

Data and materials availability:

All data needed to evaluate the conclusions in this paper are present in the paper and/or the supplementary materials. The data can be requested from G.L. and X.L. (corresponding authors).

Reference

[1] M. A. Green, A. Ho-Baillie, H. J. Snaith, *Nature photonics* **2014**, 8, 506.

[2] A. Kojima, K. Teshima, Y. Shirai, T. Miyasaka, *Journal of the American Chemical Society* **2009**, 131, 6050.

[3] H. J. Snaith, *The journal of physical chemistry letters* **2013**, 4, 3623.

[4] a) D. H. Cao, C. C. Stoumpos, O. K. Farha, J. T. Hupp, M. G. Kanatzidis, *Journal of the American Chemical Society* **2015**, 137, 7843; b) A. Krishna, S. Gottis, M. K. Nazeeruddin, F. Sauvage, *Advanced Functional Materials* **2019**, 29; c) H. Lai, B. Kan, T. Liu, N. Zheng, Z. Xie, T. Zhou, X. Wan, X. Zhang, Y. Liu, Y. Chen, *J Am Chem Soc* **2018**, 140, 11639; d) C. Ma, C. Leng, Y. Ji, X. Wei, K. Sun, L. Tang, J. Yang, W. Luo, C. Li, Y. Deng, S. Feng, J. Shen, S. Lu, C. Du, H. Shi, *Nanoscale* **2016**, 8, 18309; e) R. Yang, R. Li, Y. Cao, Y. Wei, Y. Miao, W. L. Tan, X. Jiao, H. Chen, L. Zhang, Q. Chen, H. Zhang, W. Zou, Y. Wang, M. Yang, C. Yi, N. Wang, F. Gao, C. R. McNeill, T. Qin, J. Wang, W. Huang, *Adv Mater* **2018**, 30, e1804771.

[5] a) G.-W. Kim, G. Kang, M. Malekshahi Byranvand, G.-Y. Lee, T. Park, *ACS applied materials & interfaces* **2017**, 9, 27720; b) J. Lee, M. Malekshahi Byranvand, G. Kang, S. Y. Son, S.

Song, G.-W. Kim, T. Park, *Journal of the American Chemical Society* **2017**, 139, 12175.

[6] a) J. H. Noh, S. H. Im, J. H. Heo, T. N. Mandal, S. I. Seok, *Nano letters* **2013**, 13, 1764; b) N. J. Jeon, J. H. Noh, W. S. Yang, Y. C. Kim, S. Ryu, J. Seo, S. I. Seok, *Nature* **2015**, 517, 476.

[7] N. R. E. Laboratory, **2020**.

[8] M. Ohring, *Materials science of thin films*, Elsevier, **2001**.

[9] a) S. Wagner, in *Vapour Growth and Epitaxy*, Elsevier **1975**, p. 113; b) G. Bauhuis, P. Mulder, E. Haverkamp, J. Huijben, J. Schermer, *Solar Energy Materials and Solar Cells* **2009**, 93, 1488; c) R. M. France, F. Dimroth, T. J. Grassman, R. R. King, *MRS Bulletin* **2016**, 41, 202; d) K. Yamaguchi, N. Nakayama, H. Matsumoto, S. Ikegami, *Japanese Journal of Applied Physics* **1977**, 16, 1203; e) A. Ptak, D. Friedman, S. Kurtz, R. Reedy, *Journal of Applied Physics* **2005**, 98, 094501; f) S. P. Tobin, S. Vernon, C. Bajgar, S. Wojtczuk, M. R. Melloch, A. Keshavarzi, T. Stellwag, S. Venkatensan, M. Lundstrom, K. A. Emery, *IEEE Transactions on Electron Devices* **1990**, 37, 469; g) T. Sugaya, A. Takeda, R. Oshima, K. Matsubara, S. Niki, Y. Okano, *Journal of crystal growth* **2013**, 378, 576.

[10] a) M. V. Kelso, N. K. Mahenderkar, Q. Chen, J. Z. Tubbesing, J. A. Switzer, *Science* **2019**, 364, 166; b) G. Tang, P. You, Q. Tai, A. Yang, J. Cao, F. Zheng, Z. Zhou, J. Zhao, P. K. L. Chan, F. Yan, *Advanced Materials* **2019**, 31, 1807689; c) Y. Chen, Y. Lei, Y. Li, Y. Yu, J. Cai, M.-H. Chiu, R. Rao, Y. Gu, C. Wang, W. Choi, *Nature* **2020**, 577, 209; d) L. Ji, H.-Y. Hsu, J. C. Lee, A. J. Bard, E. T. Yu, *Nano letters* **2018**, 18, 994; e) J. Cao, G. Tang, P. You, T. Wang, F. Zheng, J. Zhao, F. Yan, *Advanced Functional Materials* **2020**, 30, 2002358; f) Y. Wang, L. Gao, Y. Yang, Y. Xiang, Z. Chen, Y. Dong, H. Zhou, Z. Cai, G.-C. Wang, J. Shi, *Physical Review Materials* **2018**, 2, 076002; g) Y. Wang, F. Yang, X. Li, F. Ru, P. Liu, L. Wang, W. Ji, J. Xia, X. Meng, *Advanced Functional Materials* **2019**, 29, 1904913; h) J. Jiang, X. Sun, X. Chen, B. Wang, Z. Chen, Y. Hu, Y. Guo, L. Zhang, Y. Ma, L. Gao, F. Zheng, L. Jin, M. Chen, Z. Ma, Y. Zhou, N. P. Padture, K. Beach, H. Terrones, Y. Shi, D. Gall, T. M. Lu, E. Wertz, J. Feng, J. Shi, *Nat Commun* **2019**, 10, 4145; i) M. Sytnyk, A. A. Yousefi-Amin, T. Freund, A. Prihoda, K. Götz, T. Unruh, C. Harreiss, J. Will, E. Spiecker, J. Levchuk, *Advanced Functional Materials* **2020**, 30, 2004612.

[11] a) D. Bi, C. Yi, J. Luo, J.-D. Décoppet, F. Zhang, S. M. Zakeeruddin, X. Li, A. Hagfeldt, M. Grätzel, *Nature Energy* **2016**, 1, 1; b) F. Hermerschmidt, F. Mathies, V. R. Schröder, C. Rehermann, N. Z. Morales, E. L. Unger, E. J. List-Kratochvil, *Materials Horizons* **2020**, 7, 1773.

[12] a) E. Shi, B. Yuan, S. B. Shiring, Y. Gao, Y. Guo, C. Su, M. Lai, P. Yang, J. Kong, B. M. Savoie, *Nature* **2020**, 580, 614; b) J. Wang, S. Luo, Y. Lin, Y. Chen, Y. Deng, Z. Li, K. Meng, G. Chen, T. Huang, S. Xiao, *Nature communications* **2020**, 11, 1; c) J.-W. Lee, S. Tan, T.-H. Han, R. Wang, L. Zhang, C. Park, M. Yoon, C. Choi, M. Xu, M. E. Liao, *Nature Communications* **2020**, 11, 1.

[13] a) Q. Jiang, Z. Chu, P. Wang, X. Yang, H. Liu, Y. Wang, Z. Yin, J. Wu, X. Zhang, J. You, *Adv Mater* **2017**, 29; b) Q. Jiang, Y. Zhao, X. Zhang, X. Yang, Y. Chen, Z. Chu, Q. Ye, X. Li, Z. Yin, J. You, *Nature Photonics* **2019**, 13, 460.

[14] K. Yan, M. Long, T. Zhang, Z. Wei, H. Chen, S. Yang, J. Xu, *Journal of the American Chemical Society* **2015**, 137, 4460.

[15] S. Yang, Y. C. Zheng, Y. Hou, X. Chen, Y. Chen, Y. Wang, H. Zhao, H. G. Yang, *Chemistry of Materials* **2014**, 26, 6705.

[16] O. E. Lanford, S. J. Kiehl, *Journal of the American Chemical Society* **1941**, 63, 667.

[17] a) C. Fei, L. Guo, B. Li, R. Zhang, H. Fu, J. Tian, G. Cao, *Nano Energy* **2016**, 27, 17; b) R. Munir, A. D. Sheikh, M. Abdelsamie, H. Hu, L. Yu, K. Zhao, T. Kim, O. E. Tall, R. Li, D. M. Smilgies, *Advanced Materials* **2017**, 29, 1604113.

[18] C. Rehermann, A. Merdasa, K. Suchan, V. Schro¨der, F. Mathies, E. L. Unger, *ACS Applied Materials & Interfaces* **2020**, 12, 30343.

[19] R. Quintero-Bermudez, A. Gold-Parker, A. H. Proppe, R. Munir, Z. Yang, S. O. Kelley, A. Amassian, M. F. Toney, E. H. Sargent, *Nature materials* **2018**, 17, 900.

[20] a) J. W. Mullin, *Crystallization*, Elsevier, **2001**; b) R. Boistelle, J. Astier, *Journal of Crystal Growth* **1988**, 90, 14.

[21] a) M. Qin, K. Tse, T. K. Lau, Y. Li, C. J. Su, G. Yang, J. Chen, J. Zhu, U. S. Jeng, G. Li, *Advanced Materials* **2019**, 31, 1901284; b) M. Qin, H. Xue, H. Zhang, H. Hu, K. Liu, Y. Li, Z. Qin, J. Ma, H. Zhu, K. Yan, *Advanced Materials* **2020**, 32, 2004630.

[22] U. Rau, *Physical Review B* **2007**, 76, 085303.

[23] S. Mahesh, J. M. Ball, R. D. J. Oliver, D. P. McMeekin, P. K. Nayak, M. B. Johnston, H. J. Snaith, *Energy & Environmental Science* **2020**, 13, 258.

[24] G. Zheng, C. Zhu, J. Ma, X. Zhang, G. Tang, R. Li, Y. Chen, L. Li, J. Hu, J. Hong, *Nature communications* **2018**, 9, 1.

[25] Q. Jiang, Z. Chu, P. Wang, X. Yang, H. Liu, Y. Wang, Z. Yin, J. Wu, X. Zhang, J. You, *Advanced materials* **2017**, 29, 1703852.

[26] A. Mei, X. Li, L. Liu, Z. Ku, T. Liu, Y. Rong, M. Xu, M. Hu, J. Chen, Y. Yang, *science* **2014**, 345, 295.